www.acsami.org

Research Article

Hyaluronic Acid-Based Nanomotors: Crossing Mucosal Barriers to Tackle Antimicrobial Resistance

Noelia Ruiz-González,[⊥] Daniel Sánchez-deAlcázar,[⊥] David Esporrín-Ubieto, Valerio Di Carlo, and Samuel Sánchez*

Cite This: *ACS Appl. Mater. Interfaces* 2025, 17, 27988−27999

Read Online

ACCESS | Metrics & More | Article Recommendations | SI Supporting Information

ABSTRACT: Bacterial infections pose a significant global health challenge aggravated by the rise of antimicrobial resistance (AMR). Among the obstacles preventing effective treatment are biological barriers (BBs) within the body such as the mucus layer. These BBs trap antimicrobials, necessitating higher doses and ultimately accelerating AMR. Addressing this issue requires innovative therapeutic strategies capable of bypassing BBs to deliver drugs more effectively. Here, we present nanomotors (NMs) based on hyaluronic acid (HA)- and urease-nanogels (NGs) as a solution to navigate effectively in viscous media by catalyzing the decomposition of urea into ammonium and carbon dioxide. These HA-based nanomotors (HA-NMs) were loaded with chloramphenicol (CHL) antibiotic and demonstrated superior antimicrobial activity against *Escherichia coli* (*E. coli*) compared to mesoporous silica NMs (MSNP-NMs), a reference in the field of NMs. Moreover, using an in vitro transwell model we evaluated the ability of HA-NMs to penetrate mucin barriers, effectively reducing *E. coli* proliferation, whereas the free antibiotic did not reduce bacteria proliferation. The optical density reduction at 24 h was over ten times greater than with free CHL. These organic-based enzyme-powered NMs represent a significant advancement in drug delivery, offering a promising approach to combat AMR while addressing the challenges of crossing complex BBs.

KEYWORDS: nanogels, nanomotors, biological barriers, bacterial infections, drug delivery
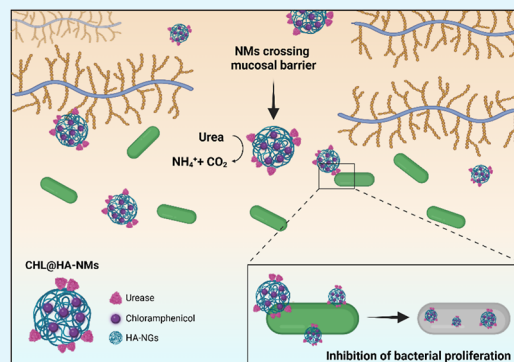
1. INTRODUCTION

The World Health Organization reported that bacterial infection caused more than 1.27 billion deaths in 2019, representing 25.6% of global mortality worldwide.[1] The growing threat of antimicrobial resistance (AMR) has intensified this crisis, leading to the failure of conventional treatments and a rise in infections that are becoming progressively harder to manage, posing a significant burden on healthcare systems.[2−4] Therefore, there is a pressing need to develop innovative strategies to tackle this global silent threat.[5]

In this regard, one of the key challenges involves the development of effective therapies for infections present in biological areas with difficult access due to biological barriers (BBs),[6−8] like mucus layer,[8] which can be found in the urinary tract, eye, vagina, and several biofilms.[9] These barriers protect us from external pathogens but also limit the diffusion of drugs, reducing the dose that reaches the infection area. Therefore, the quantity and dosage of antibiotics must be increased in these cases to achieve effective therapy fostering the AMR.

Despite the development of nanoparticles (NPs) for biomedical applications, their efficacy remains very low.[10] In recent years, enzyme-powered nanomotors (NMs) have emerged as a promising tool for the future in nanomedicine.[11,12] These NMs use the power of enzymatic catalysis to self-propel

NPs in complex biological media, showing enhanced capabilities for drug delivery[13−15] and tissue penetration[16−18] among other applications.[19,20]

Traditionally, the design of enzyme-powered NMs has been focused on the use of inorganic NPs as core structures for their fabrication.[13,17,20−29] These NMs actively interact and modulate different BBs, such as synovial fluid[26] or mucus,[29] showing significant promise for their applications for clinical uses.

Nowadays, the field of NMs is expanding to explore more biodegradable and biocompatible materials for their fabrication based on organic NPs,[30−35] minimizing potential toxicity.[33,36] This evolution in material design aligns with the concept of nanoarchitectonics, which aims to construct functional systems by organizing nanomaterials into integrated architectures.[37,38] Nanogels (NGs) emerged as a versatile platform for advanced drug delivery systems as their easy surface tuneability and effective drug loading and release capacity[39,40] position them as
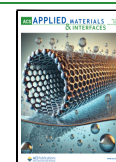
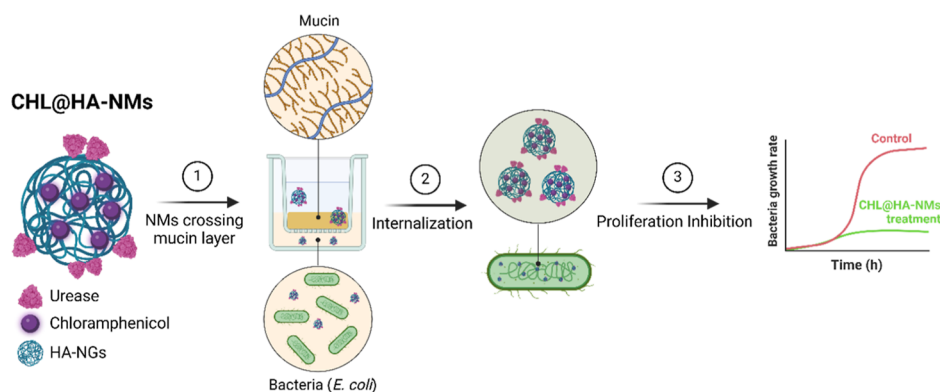**Scheme 1. Chloramphenicol-Loaded HA-Based Powered NMs (CHL@HA-NMs) Effectively Cross Mucin Barriers Using a Transwell Model[a]**

[a]These nanomotors demonstrate enhanced internalization in bacteria, leading to efficient inhibition of bacterial proliferation. Their ability to navigate biological barriers and target bacterial cells showcases their potential as a powerful strategy for combating infections in hard-to-reach areas. Created in BioRender. Sánchez, S. (2025) https://BioRender.com/t8jawxi.

an ideal core for enzyme-powered NMs.[41] Among the different materials that could be used, hyaluronic acid (HA) stands out as a widely used biomolecule due to its excellent intrinsic properties.[42] It is composed of repeating units of glucuronic acid and N-acetylglucosamine found in the human body's connective and epithelial tissues.[43] It is highly biocompatible and biodegradable, breaking down naturally without leaving toxic residues, making it ideal for drug delivery systems, such as its use in NGs formulation.[44,45]

Previously, several works have reported the use of NMs to treat bacterial infections, demonstrating their potential to tackle AMR.[46−50] All-in-all, those approaches have provided insight into the challenges we need to address in subsequent research. The combination of biodegradable nanomaterials and the ability to cross BBs represents a considerable challenge that must be addressed to develop effective solutions, enabling targeted delivery and sustained therapeutic effects.

In this work, we present an innovative class of urease-powered NMs based on HA nanogels (HA-NGs), designed to navigate challenging viscous environments. By chemically modifying HA with methacrylic groups, we engineered HA-NGs and functionalized them with urease. We evaluated their motion both individually and collectively and demonstrated robust self-propulsion capabilities. As a proof-of-concept, we loaded the antibiotic chloramphenicol (CHL) into HA-based nanomotors (HA-NMs), achieving substantial antimicrobial efficacy. Notably, in an in vitro mucin transwell model that mimics BBs, CHL-loaded HA-NMs (CHL@HA-NMs) exhibited superior penetration through a viscous layer and enhanced bacterial growing inhibition compared to free CHL (Scheme 1). These results highlight the potential of HA-NMs as a groundbreaking platform for targeted drug delivery in challenging biological environments.

2. RESULTS AND DISCUSSION

2.1. Synthesis and Characterization of HA-NPs. We explored the preparation of covalently cross-linked HA-based NGs, as the core for the NMs (Figure 1A). For that, we modified HA with methacrylic anhydride (MA) to introduce vinyl groups into the polymeric chains (Figure S1) for their posterior use in the formation of the NGs. We confirmed the methacrylation by ^{1}H NMR spectrum, which evidences the structural changes of

the molecule with peaks emerging at 6.1, 5.7, and 1.9 ppm, corresponding to the protons of the methylene (a, b in the NMR spectra) and methyl (c in the NMR spectra) groups, respectively, in contrast to the spectrum of unmodified HA (Figure 1B). Subsequently, we prepared HA-NGs by copolymerizing the methacrylated HA with the cross-linker diethylene glycol dimethacrylate (DEGDA), in an aqueous solution at 70 °C for 2 h. This process was initiated by potassium persulfate (KPS), and the reaction took place under an argon atmosphere. We purified the final material with a dialysis membrane of 50 kDa against ultrapure water with water change twice per day for a week. The Fourier transform infrared attenuated total reflectance (FTIR-ATR) spectra of methacrylated hyaluronic acid (MAHA), DEGDA, and the HA-NGs (Figure 1C) exhibited a transmission band at 3200 cm^{-1} for HA-NGs, associated with the stretching of hydroxyl groups of MAHA. Additionally, a peak at 1700 cm^{-1} indicates the stretching of the carbonyl group from DEGDA, confirming that the NGs were formed through the cross-linking reaction between MAHA and DEGDA. We further confirmed the shape and morphology of the NGs by transmission electron microscopy (TEM) (Figure S2) and dispersity by scanning electron microscopy (SEM) (Figure 1D), ratifying a narrow size distribution with a diameter ca. 54.1 ± 5.1 nm (N = 500) (Figure 1E). As an alternative strategy for HA-NPs synthesis, we prepared HA-based NPs via self-assembly HA (20 kDa) with p-L-arginine (5800 Da), with few modifications from the reported literature (Supporting Information, Figure S3 and Tables S1−S3).[51] We successfully obtained highly monodisperse NPs with a 485.0 ± 27.01 nm diameter using an injection speed rate of 0.67 mL min^{-1}.

2.2. HA-NMs Fabrication. To fabricate the HA-based NMs, we chemically linked urease onto the surface of HA-NGs and HA-NPs via click-chemistry of the 1-ethyl-3-(3-(dimethylamino)propyl)carbodiimide and N-hydroxysuccinimide (EDC/NHS) (Figure 2A). EDC/NHS allowed the formation of chemical junctions between the amino groups of the lysine from the urease with the carboxylic groups of the HA. For HA-NPs, we observed a lack of stability after their covalent surface functionalization with urease to form NMs, i.e., aggregation and loss of monodispersity. We attributed this undesired effect to the strong chemical bonds used for anchoring the enzyme, which affected the physical forces essential to maintaining the structural integrity of the assembled NPs.
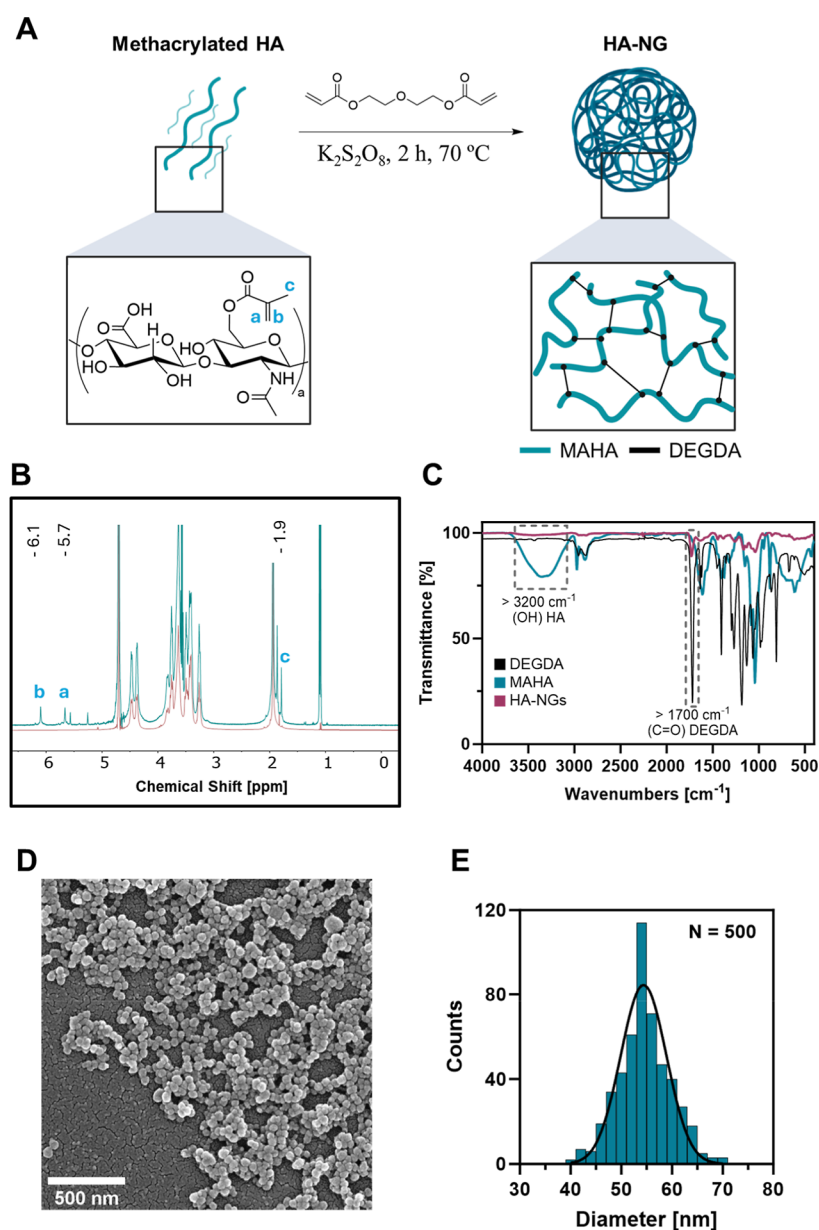
Figure 1. Fabrication and morphological characterization of HA-NGs. (A) Synthesis workflow of HA-NGs. Part of the figure was created in BioRender. Sánchez, S. (2025) https://BioRender.com/mz13gph. (B) ^{1}H NMR spectra (400 MHz, D_2O) of HA (pink) and MAHA (blue). (C) FTIR-ATR spectra (4000−400 cm^{-1}) of DEGDA (black), MAHA (blue), and HA-NGs (pink). (D) SEM image of HA-NGs. Scale bar: 500 nm. (E) Diameter histogram of HA-NGs obtained by SEM ($N = 500$).

Consequently, this strategy was considered to be unsuitable for further experiments. In contrast, for HA-NGs we proved the successful preparation of the NMs by dynamic light scattering (DLS), observing an increase in the overall diameter after enzyme functionalization (Figure 2B). The results indicated a highly monodisperse population, as made evident by the narrow peak width in both samples. The formation of HA-NMs resulted in a noticeable increase in the z-average size with a narrow polydispersity [Figure S4A, (i,ii)], which increased from 217 ± 2 nm to 541 ± 24 nm, confirming the successful enzyme conjugation on the HA-NMs. It is worth noting that this striking change of size can be attributed to enzyme clustering since the size of a single enzyme is 12.1 nm according to crystallography calculations (Figure S4B). Therefore, the NMs would not simply have double the size of the NGs. In addition, we hypothesize that clustering formation could play a key role in

the asymmetry formation of NMs.[52] It is important to mention that while the HA-NGs diameter determined by DLS was around 217 ± 2 nm, the particle size measured by TEM and SEM was approximately 55 nm (Figures 1D and S2). This discrepancy is attributed to dehydration of the NGs in the dry state.

Regarding the surface charge of the NGs, the z-potential of HA-NGs was -51.6 ± 0.3 mV in ultrapure water, attributed to the presence of carboxylic groups on their surface. After the covalent attachment of urease, the surface charge shifted to -18.6 ± 0.5 mV (Figure 2C). This change toward more positive values indicates the successful attachment of the enzyme to the NGs' surface, as the surface charge of urease, determined computationally, is on average -1.5 ± 0.03 kcal mol^{-1} × 10^{-1} (Figure S4B). The enzyme attachment was also confirmed using
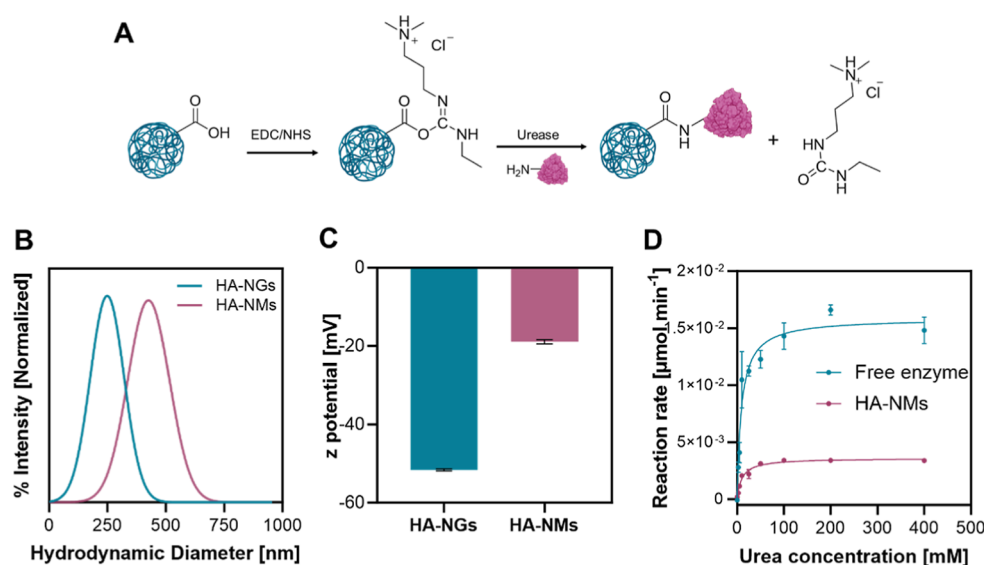
Figure 2. Synthesis and characterization of HA-NMs. (A) Schematic representation of the step-by-step fabrication process of HA-NMs. Part of the figure was created in BioRender. Sánchez, S. (2025) https://BioRender.com/zsifzg9. (B) Hydrodynamic diameter of HA-NGs and HA-NMS. (C) Surface charge of HA-NGs and HA-NMs. (D) Enzymatic reaction rate of free urease and urease anchored on the surface of HA-NGs at different urea concentrations (0, 2.5, 5, 10, 25, 50, 100, 200, and 400 mM). The data were fitted to the Michaelis−Menten equation to obtain the kinetic parameters $(V = V_{max}[urea]/K_m + [urea])$. ($N = 3$, data presented as mean $\pm$ SD).

a BCA kit assay. The amount of urease bounded was 98.2 ± 1.27 μg mL^{-1} (Figure S4C).

Moreover, we determined the enzymatic activity of free urease and that on the surface of the NMs, at different urea concentrations, and adjusted them to the Michaelis−Menten model (Figure 2D). The enzymatic kinetic parameters of HA-NG NMs displayed a slightly lower k_{cat}^{app} and higher K_m^{app} compared to the free enzyme resulting in a reduced specificity constant, i.e., 9.3 ± 2.7 and 7.9 ± 1.0 mM^{-1} s^{-1}, which diminishes the enzyme's efficiency in converting substrates into products (Table S4). This slight reduction is a common occurrence when enzymes are immobilized due mainly to the restriction of overall protein structure and substrate access to the active center.[53]

Finally, we performed FTIR analysis of the resulting HA-NMs (Figure S4D). Although no new bands were observed due to the overlapping signals from amine, hydroxyl, and carboxyl groups in both urease and the HA polymer, the spectra confirmed the presence of these functional groups. We confirm that after urease anchoring the NGs remain stable, as all functional groups from the initial HA-NGs are still present in the spectrum, displaying a similar pattern to that observed in Figure 1C.

2.3. Motion Analysis of HA-NMs. We evaluated the motion of HA-NMs at the single and collective level in the presence of different urea concentrations. For the single particle tracking, we evaluated the self-propelled capabilities of HA-NMs and recorded their trajectories in the presence of 0 and 100 mM of urea (Figure 3A and Video S1). The mean squared displacement (MSD) (Figure 3B) was derived from the particle trajectories for single particle tracking. HA-NMs with and without urea exhibited a linear MSD, indicative of diffusive motion, typically observed for nanoscale particles.[54] The covalent bonds between the enzymes (urease) and HA-NGs surface via EDC/NHS led to the asymmetric enzyme distribution on the particle's surface, which produces a propulsive force that drives NMs motion, as previously reported.[55−57]

We observed an increase in the MSD slope in the case of NMs in the presence of urea, indicating enhanced diffusion. Notably, the MSD slope values for HA-NMs were higher, reaching approximately 6.7 μm^2 after 1.5 s, compared to other urease-powered NMs of similar diameters constructed from inorganic materials such as mesoporous silica-based NMs (MSNP-NMs), which exhibited MSD values in the range of 3−3.5 μm^2 at same time point.[13,17,47,58] We attributed these differences to several factors, such as surface interactions between the HA polymer and the aqueous surrounding media, propulsion efficiency, and hydrophilicity of the materials, highlighting the benefit of using organic-based NMs. Typically, MSNP-based NMs, being more rigid and hydrophobic than HA, tend to exhibit lower diffusion rates, whereas the flexibility of polymers such as HA enhances the propulsion efficiency, resulting in a steeper MSD slope. Besides, we observed a significant increase in the diffusion coefficient of HA-NMs in the presence of urea (Figure 3C), rising from 1.11 ± 0.039 to 1.51 ± 0.079 μm s^{-1}. This 36% diffusion increment provides clear evidence of HA-NMs' self-propulsion capabilities, driven by the catalytic reaction of urease, which is in accordance with previous reports of urease-powered NMs.[13,17,21,47,58]

After proving the motion of HA-NMs at a single particle level, we explored their collective dynamic motion in the presence of 0, 50, 100, and 200 mM of urea (Figures 3D and S5 and Video S2). We observed an increase in the normalized covered area explored by the HA-NMs, consistent with the reported literature.[20,27] In the absence of urea, most of the HA-NMs were set onto the bottom of the Petri dish after slight diffusion. We quantified the area covered by the NMs (Figure 3E). Although the covered areas were similar in the presence of 0 mM (35.1 ± 2.0 mm^2) and 50 mM urea (35.8 ± 6.2 mm^2), we observed the formation of plumes at 50 mM urea (Figure S5). This behavior suggests that the NMs were active, consistent with previously reported characteristics of urease-based NMs.[20,59] In the presence of 100 mM urea, the area covered by the HA-NMs increased to 39.1 ± 3.5 mm^2 after 30 s (1.25-fold increase
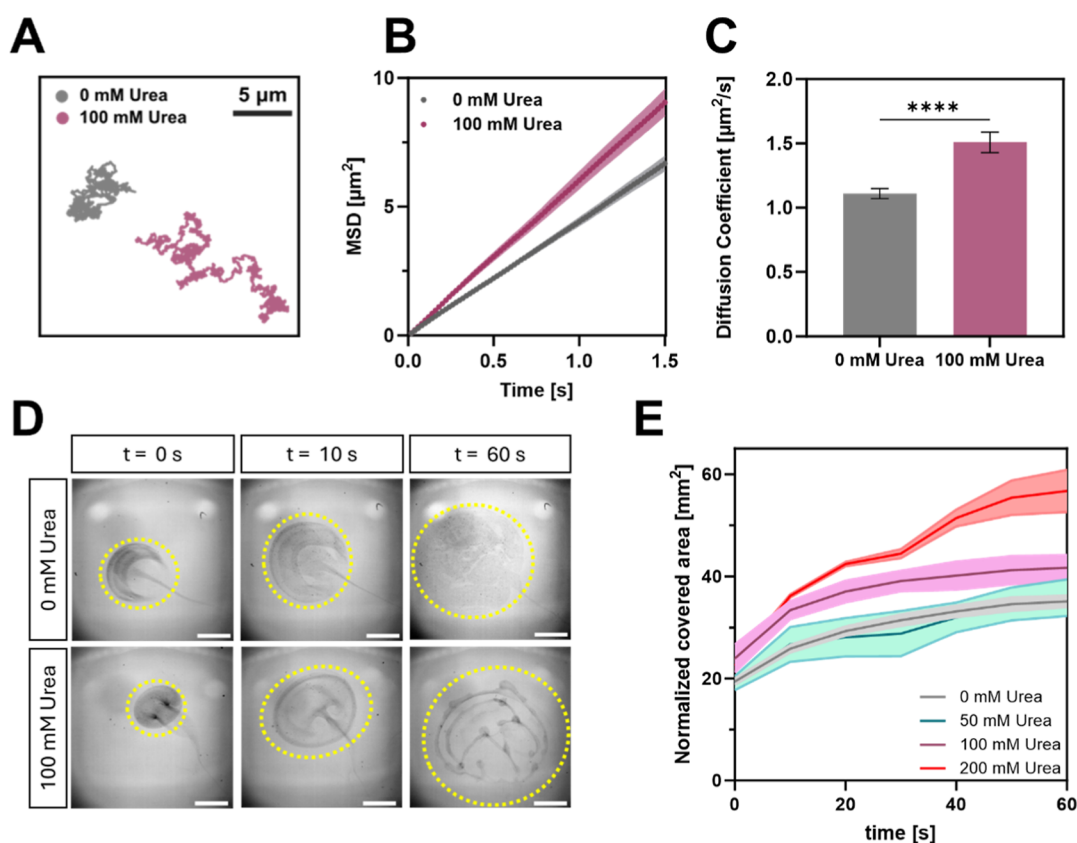
Figure 3. Motion analysis of HA-NMs at a single and collective particle level in PB. (A) Representative tracking trajectories of HA-NMs, with different urea concentrations (0 mM, gray; 100 mM, pink). (B) MSDs of HA-NMs in the absence and presence of urea (100 mM urea). (C) Diffusion coefficients obtained by MSD analysis. Results are shown as mean $\pm$ SE. Asterisks denote a significant difference among conditions with ****$p \le$ 0.0001, N = 20; (D) video screenshots of collective displacement of HA-NMs with urea (100 mM urea) and without urea. Scale bar = 1 μm. (E) Normalized area covered by HA-NMs between times t = 0 and t = 60 s.

compared to 0 mM urea) and to 41.7 $\pm$ 4.3 mm^2 after 60 s, representing a 1.18-fold increase. When the urea concentration was raised to 200 mM, the HA-NMs spread more rapidly, covering 44.5 $\pm$ 1.6 mm^2 at 30 s (1.42-fold increase) and 56.7 $\pm$ 7.2 mm^2 at 60 s (1.6-fold increase). These results suggest that the active propulsion of HA-NMs, enhanced by fluid mixing induced by urea, significantly promotes their expansion and collective displacement in a concentration-dependent manner.

2.4. Evaluation of the Antimicrobial Effect of CHL@HA-NMs. Chloramphenicol (CHL) is a broad-spectrum antibiotic that inhibits bacterial protein synthesis, by preventing peptide bond formation, and acts as a bacteriostatic agent for most organisms.[60] CHL is typically used for ophthalmological and ear infection treatments. However, its high hydrophobicity and low capacity to cross BBs limit the therapeutic efficiency.[8,61] We loaded CHL, as a drug model, into our HA-NMs to improve the bioavailability of the drug. Hence, we have evaluated HA-NMs as drug delivery systems focusing on the transport of CHL and the inhibition of bacterial growth and compared them to MSNP-NMs.[13,21] We prepared MSNP via the Stöber method with slight modifications of the synthetic procedure (more detail in the Experimental Section). Later, we incorporated primary amino groups to anchor the urease, obtaining MSNP-NMs.[26,28,29] We characterized the MSNP-NMs, observing an overall size of ca. 450 nm diameter by SEM, surface charge of -12.6 ± 0.9 mV, and $91.8 \pm 2.14\,\mu$g mL^{-1} of urease attached by BCA (Figure S6). We loaded CHL in both NMs, achieving an encapsulation efficiency of $32.2 \pm 0.5\%$ ($327.02 \pm 3.08\,\mu$g) for CHL@HA-

NMs and $10.8 \pm 1.2\%$ ($107.5 \pm 12.1\,\mu$g) for CHL@MSNP-NMs after 24 h (Figure 4A).

The higher encapsulation of CHL in HA-NMs compared to that in MSNP-NMs can be attributed to the structural and physicochemical differences between these two materials. HA-NGs exhibit a highly hydrated, flexible, and expandable polymeric structure that allows them to absorb significant amounts of water, which facilitates the solubilization and retention of drugs. Moreover, the drug-loading capacity in NGs can be chemically tuned to optimize the matrix or surface interaction with the drug, as well as network structure permeability, thereby maximizing the encapsulation efficiency of CHL.[62] We observed around 30% ($65.01 \pm 11.43\,\mu$g) of CHL released from the HA-NMs after 24 h. This value is in line with reported literature for similar HA-NGs systems that load hydrophobic drugs, such as doxorubicin.[63] The antimicrobial efficacy of CHL@HA-NMs and CHL@MSNP-NMs was assessed against a nonpathogenic strain of *E. coli*. Minimum inhibitory concentration (MIC) values were determined by measuring the optical density (OD) at 600 nm in the absence or presence of urea (100 mM urea in PBS) and exploring a range of NMs (CHL@HA-NMs and CHL@MSNP-NMs) concentrations of 0, 5, 10, 20, and 50 μg mL^{-1} (Figure 4B). The measurements were conducted at different time points, specifically at 4, 18, and 24 h. As observed after 24 h (Figure 4C and Table S5), bacterial proliferation increased significantly over time for the lowest concentration of CHL@HA-NMs, 5 and 10 μg mL^{-1}, but not much for the higher concentrations, 20
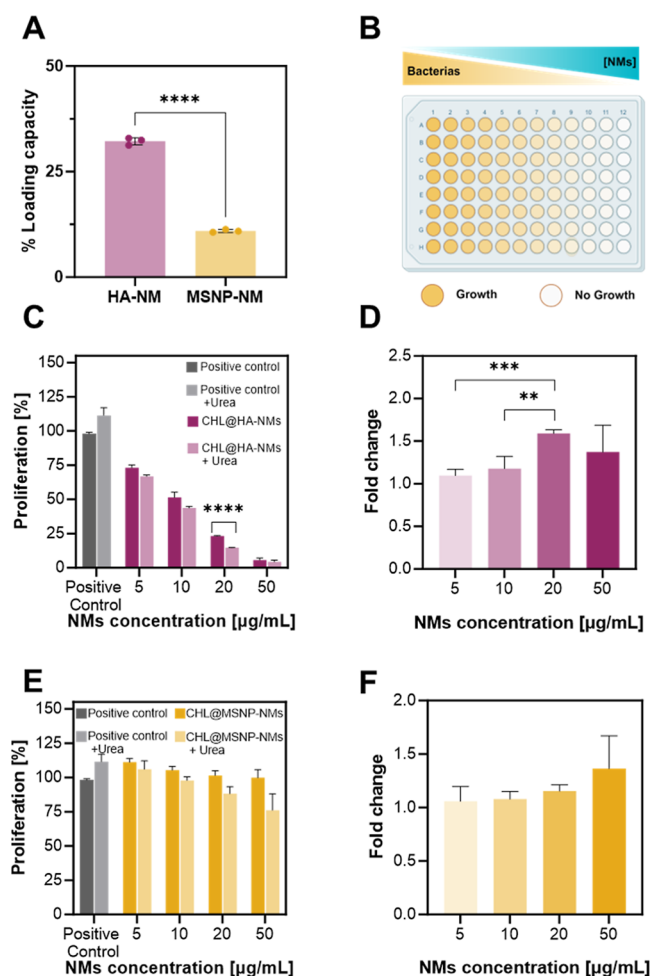
Figure 4. CHL payloads and antimicrobial activity. (A) Drug-loading capacity of CHL into HA-NMs and MSNP-NMs. (B) Scheme showing experimental design of biological activity assays. Briefly, 10^5 bacterial cells, the antibiotic CHL, CHL@HA-NMs, or CHL@MSNP-NMs (0 −50 μg mL^{-1}) were added to a 96-well plate and incubated at room temperature. Created in BioRender. Sánchez, S. (2025) https://BioRender.com/cr0v9sb. (C) Proliferation rate (%) of nonpathogenic *E. coli* bacteria in contact with different concentrations of CHL@HA-NMs in the presence or absence of urea (100 mM urea in phosphate-buffered saline (PBS)) at 24 h. (D) Synergistic effect of ammonium produced by HA-NMs combined with the antibiotic in the proliferation. (E) Proliferation rate of nonpathogenic *E. coli* bacteria in contact with different concentrations of CHL@MSNP-NMs in the presence or absence of urea (100 mM urea in PBS). (F) Synergistic effect of ammonium produced by MSNP-NMs combined with the antibiotic in the proliferation. Data are presented as mean ± SD. Statistics: **$p \leq 0.01$, ***$p \leq 0.001$, and ****$p \leq 0.0001$.

and 50 μg mL^{-1}. The most effective CHL@HA-NMs concentration to inhibit the bacteria proliferation was 50 μg mL^{-1} (equivalent to 0.87 μg of CHL), although significant inhibition was also observed at 20 μg mL^{-1}, which effectively controlled proliferation up to 24 h. It is worth mentioning that the catalytic products of urea hydrolysis resulted in a synergic effect with the drug, reducing the proliferation even at the lowest NMs concentration, i.e., 1−1.5-fold proliferation reduction for all tested concentrations of HA-NMs at 24 h (Figure 4D). We compared the capacity of MSNP-NMs (already tested in our group)[48] and HA-NMs as drug delivery systems for antimicrobial effect. Conversely, as displayed in Figure 4E and Table S6, we found that CHL@MSNP-NMs were ineffective at any

concentration at 24 h, likely due to their lower drug-loading capacity. Noticeably, the synergic effect between ammonium and the drug displayed the same trend for MSNP-NMs as it was observed for HA-NMs (Figure 4E). Moreover, we also observed no significant difference in the fold change synergistic effect of ammonium for the case of MSNP-NMs (Figure 4F). Data corresponding to the earlier time points (4 and 18 h) for CHL@HA-NMs are provided in Figure S7 and Tables S7, S8 and for CHL@MSNP-NM in Figure S8 and Tables S9, S10, which are in line with the results at 24 h. We observed a similar antimicrobial profile for the free CHL (Figure S9 and Tables S11−S13).

Considering the potential capacities of CHL@HA-NMs for inhibiting bacteria proliferation, we aim to explore the HA-NMs' interaction with bacteria. Therefore, we assessed the internalization of the HA-NMs inside the bacteria by confocal microscopy (Figure 5). For that, we labeled the HA-NMs with
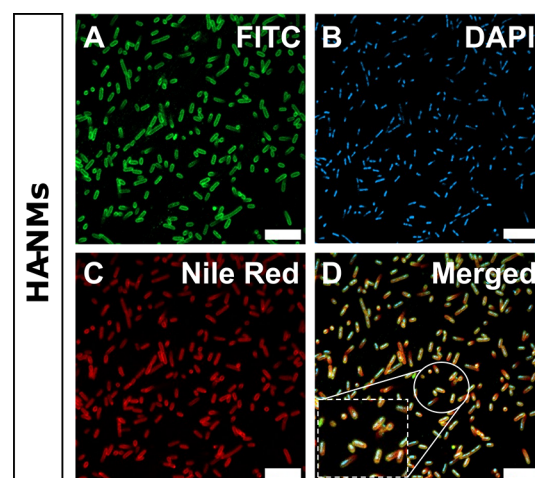

Figure 5. HA-NMs internalization in *E. coli* by confocal microscopy. Immunofluorescence staining of (A) HA-NMs labeled with FITC (green), (B) DNA (blue, DAPI), and (C) cell membrane (red, Nile Red). (D) Merged confocal microscopy image from A, B, and C with a zoomed-in inset. Scale bars: 10 μm.

fluorescein isothiocyanate (FITC), reacting the FITC with the amine groups of ureases prior to attachment in the NGs (Figure 5A) and staining the bacteria with 4′,6-diamidino-2-phenyl-indole, dihydrochloride (DAPI) (Figure 5B) and Nile red (Figure 5C), which bind to the DNA and membrane, respectively.

In Figure 5D, we show a colocalization of fluorophores, suggesting that HA-NMs bind and internalize into bacteria cells. Furthermore, we observed that a significant amount was taken up in less than 2 h of incubation. We hypothesized that the polysaccharide-like structure of HA-NMs might foster their internalization inside the cells. We also evaluated the stability of the HA-NMs over time, following 24 and 72 h of incubation in the presence or absence of urea. The results showed a reduction in the intracellular presence of HA-NMs, likely due to dilution upon cell division (Figure S10).

2.5. NMs for Crossing Biological Barriers. Hydrophobic drugs often become trapped within viscous BBs, limiting their therapeutic efficacy.[64] Here, we assessed the potential of CHL@HA-NMs for crossing mucin, as a BB model, enhancing the CHL antibacterial potential. To test this, we employed an in vitro transwell system designed to mimic a mucin layer, enabling the evolution of HA-NMs to inhibit bacterial growth across such a
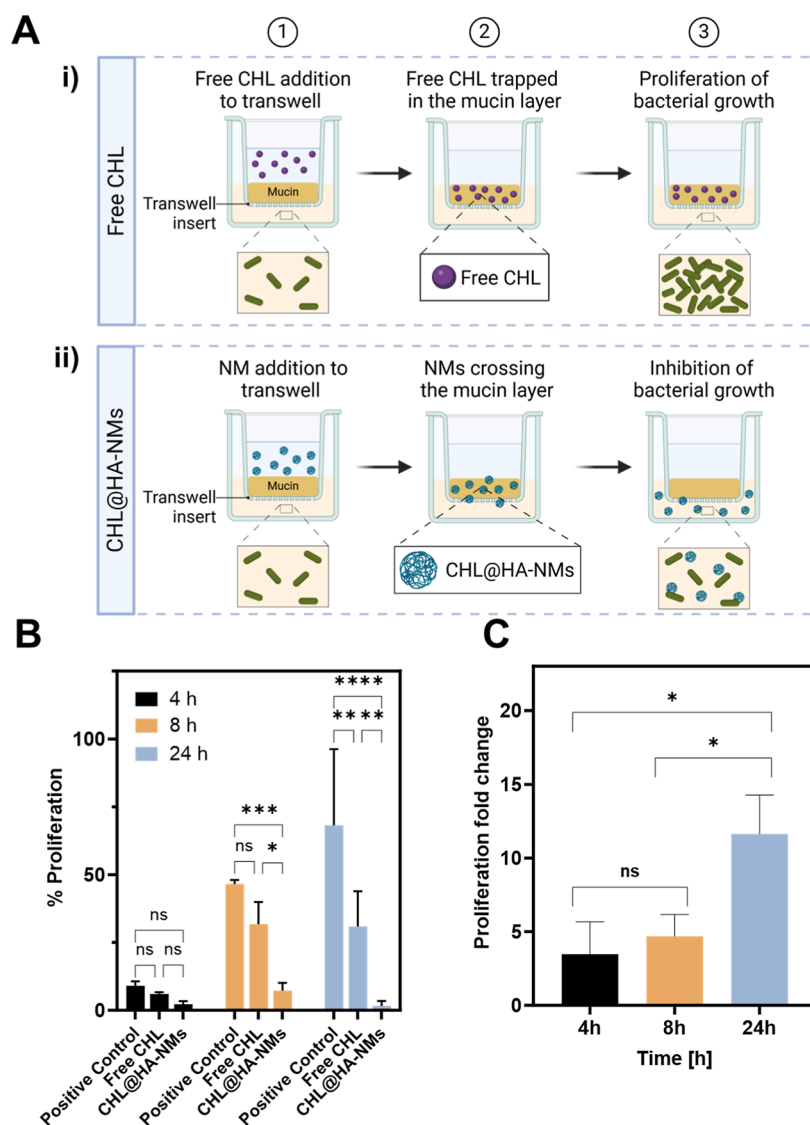
Figure 6. HA-NMs crossing mucin in a transwell model. (A) Schematic representation of the antimicrobial efficacy of (i) free CHL vs (ii) CHL@HA-NMs in a mucin barrier model. The upper panel illustrates the limited penetration and efficacy of free CHL, where the drug is trapped in the mucin layer, leading to the proliferation of bacterial growth. The lower panel depicts the enhanced penetration of CHL@HA-NMs through the mucin layer, effectively inhibiting bacterial growth. Created in BioRender. Sánchez, S. (2025) https://BioRender.com/6rts4ns. (B) Quantitative analysis of bacterial inhibition of free CHL and CHL@HA-NMs over time. (C) Fold change of bacteria proliferation comparing free CHL to CHL@HA-NMs over time. Data are presented as mean $\pm$ SD. Asterisks denote a significant difference among conditions with ns = no significant differences, $*p \leq 0.1$, $**p \leq 0.01$, $***p \leq 0.001$, $****p \leq 0.0001$.

barrier. In this setup, we cultured *E. coli* bacteria into the lower compartment of the transwell system, while the upper chamber contained a mucin layer (Figure 6A). Later, we added in the upper chamber a solution containing free CHL [Figure 6A, (i)] or CHL@HA-NMs [Figure 6A, (ii)] combined with urea (100 mM). The bacterial growth was quantified by measuring the absorbance of the liquid in the lower chamber, which directly correlates with bacterial proliferation (higher absorbance values indicate greater bacterial growth). Absorbance was monitored at 4, 8, and 24 h, and the results were plotted as a percentage of bacterial proliferation (Figure 6B). The results demonstrated that treatment with CHL@HA-NMs significantly inhibits *E. coli* proliferation compared to the control and the free CHL across different time points. At 4 h, all conditions showed minimal bacterial proliferation (~5−10%) due to lag-time of bacterial growth. Although a clear trend can be seen in the samples with CHL (both free CHL and CHL@HA-NMs), no significant

differences are observed. After 8 h, *E. coli* from the positive control group proliferated to $46.5 \pm 1.5\%$, while proliferation in the free CHL group increased to $31.7 \pm 8.2\%$, still remaining lower than the control, indicating partial antibiotic efficacy despite the mucin barrier. Notably, CHL@HA-NMs treatment further suppressed bacterial proliferation to $5.7 \pm 1.7\%$, indicating that a huge percentage of HA-NMs crossed the mucin and delivered the CHL to the bacteria cells, enhancing therapeutic efficacy over the free drug. This response was more pronounced after 24 h, where positive control peaked at $68.2 \pm 28.1\%$ proliferation. In contrast, free CHL allowed bacterial growth to progress to $30.9 \pm 12.9\%$. Notably, the presence of CHL@HA-NMs treatment resulted in negligible bacterial growth, with bacterial proliferation reduced to $2.4 \pm 1.7\%$, suggesting that the NMs provide more sustained and effective delivery of the antibiotic, with an 11.6 ± 2.6-fold greater reduction in proliferation compared to that achieved with the

free antibiotic (Figure 6C). The self-propelling CHL@HA-NMs effectively inhibited bacterial growth by enabling targeted, continuous CHL release and enhancing penetration through the mucin barrier, demonstrating their potential as an efficient method for delivering antibacterial agents across mucosal barriers.

Altogether, the HA-NM system presented in this work offers multiple strategic advantages over previously reported systems, particularly those based on inorganic materials like MSNP-NMs. These urease-powered HA-NMs exhibit superior diffusion and propulsion efficiency in the presence of fuel, facilitated by their hydrated, flexible, and lightweight structure, which allows them to navigate more easily through media compared to heavier nanostructures. Additionally, they exhibit enhanced drug-loading capacity compared with MSNP-NMs due to their amphiphilic matrix and their capability to swell. Furthermore, HA-based nanocarriers possess mucopenetrating properties, which are advantageous for developing drug delivery systems in viscous environments, such as mucus. Their autonomous propulsion removes the need for external activation (e.g., magnetic guidance or light), simplifying clinical translation and positioning HA-NMs as powerful and versatile platforms for overcoming BBs and advancing therapeutic delivery.

3. CONCLUSIONS

We demonstrated the use of HA-NMs to cross the mucin layer for antimicrobial treatment. We designed enzymatic NMs based on HA-NGs with a highly monodisperse distribution. These HA-NMs exhibited a 36% increase in coefficient diffusion at single particle level in the presence of urea, compared to passive HA-NGs. Moreover, their collective dynamic behavior demonstrated a 2-fold enhancement in the area explored by HA-NMs when exposed to urea with respect to control conditions (without urea). Furthermore, HA-NMs displayed a 2.9-fold increase in the antibiotic loading capacity compared to MSNP-NMs. As a result, CHL@HA-NMs achieved an enhanced antimicrobial effect, which effectively controlled bacteria proliferation up to 24 h compared to CHL@MSNP-NMs. More importantly, we have demonstrated that HA-NMs can penetrate and cross mucin barriers while ensuring the delivery of hydrophobic drugs such as CHL, which would otherwise remain trapped in its free form. This, together with their high capacity to internalize into the bacteria, makes HA-NMs excellent at controlling bacterial proliferation. These results highlight HA-NMs as a highly promising therapeutic strategy for bacterial infections involving viscous media, paving the way for the development of new approaches to combat the silent threat of antibiotic resistance.

4. EXPERIMENTAL SECTION

Sodium hyaluronate (HA, 20 kDa) was purchased from Lifecore Biomedical. Poly-L-arginine hydrochloride (5800 Da) was purchased from Alamanda Polymers. Methacrylic anhydride (MA, ≥94%), potassium persulfate (KPS, ≥99.0%), N-hydroxysuccinimide (NHS, 98%), urease (from *Canavalia ensiformis*, type IX, powder, 50,000−100,000 units per gram of solid), chloramphenicol (CHL ≥98%), mucin from porcine stomach (Type III), ethanol (EtOH, 99%), methanol (MeOH, 99%), hydrochloric acid (HCl, 37%), tetraethylorthosilicate (TEOS, 99%), triethanolamine (TEOA, 99%), cetyltrimethylammonium bromide (CTAB, 99%), 3-aminopropyltriethoxysilane (APTES, 99%), glutaraldehyde (GA, 25% in water), urea (99.9%), phenolsulfonphthalein (Phenol Red), Nile red (for microscopy), dimethyl sulfoxide (DMSO) ReagentPlus (≥99.5%), fluorescein isothiocyanate (FITC), Luria−Bertani (LB) broth, and

Amicon Ultra-0.5 mL (30 K) were purchased from Merck. Sodium hydroxide (NaOH, ≥98%) was purchased from Honeywell Research Chemicals. Di(ethylene glycol) diacrylate (DEGDA, 75%), 1-(3-(dimethylamino)propyl)-3-ethylcarbodiimide hydrochloride (EDC, 97%), and 96-well polystyrene microplates were purchased from Thermo Scientific. Pierce BCA Protein Assay Kit, PBS, phosphate-buffered (PB), and *E. coli* strain BL21 DE3 were purchased from Thermo Fisher. 4,6-diamidino-2-phenylindole (DAPI) was purchased from Molecular Probes (Life Technologies). Dialysis membranes Spectra/Por of 50 kD and 1000 kD were purchased from Fisher Scientific. The water used for the experiments was of type I ultrapure quality and obtained from a purification system (18.2 MΩ cm). All reagents were used as received without further purification.

4.1. Synthesis of Methacrylated HA Polymer. MAHA was synthesized as a precursor for the preparation of HA-NGs. Briefly, sodium hyaluronate (200 mg, 0.01 mmol) was dissolved in ultrapure water (20 mL). Then, MA (200 μL, 1.26 mmol) was added to the solution. The pH was adjusted to 8 using 0.1 M NaOH and the mixture reacted for 24 h at 4 °C. Then, the product was purified by recrystallization in cold EtOH. The final product, obtained with a 65% yield, was collected and stored at −20 °C until use. The product was then characterized by proton nuclear magnetic resonance (^{1}H NMR) spectroscopy using a Bruker 400 MHz equipment and Fourier Transform Infrared with attenuated total reflectance (FTIR-ATR) spectroscopy performed on a PerkinElmer Frontier equipment.

4.2. Synthesis of HA Nanogels. HA-NGs were synthesized via the chemical cross-linking of MAHA with DEGDA, as reported in the literature, with minimum modifications.[63] Briefly, MAHA (100 mg, 0.005 mmol) and DEGDA (126 mg, 0.58 mmol) were dissolved in ultrapure water (20 mL). The mixture was bubbled with argon for 1 h before starting the polymerization to avoid the formation of peroxides' undesired side products. Then, an aqueous solution of KPS previously degassed (3 mg, 0.011 mmol, 4.54 mL) was added to initiate the polymerization. The reaction was performed at 70 °C for 2 h. The final material was purified by dialysis (MWCO 50 kD) against ultrapure water. After freeze-drying the material (Christ alpha 1−4 LSC basic, working operation at −60 °C and 0.010 mbar), the resulting product was obtained as a white solid with an 80% yield.

4.3. Functionalization of HA-NGs with Urease to Fabricate HA Nanomotors. Surface modification of HA-NGs was achieved by functionalizing them with urease via click chemistry of EDC/NHS. First, the carboxylic groups on the HA-NGs (3 mg, 3 mg mL^{-1} in PB) were activated by adding EDC (1 μL, 5.70 μmol), forming an active ester intermediate. Next, NHS (2 mg, 0.017 mmol) reacted with the activated ester, generating a more stable NHS-ester intermediate, which reacts toward nucleophiles. The mixture was stirred for 30 min to ensure carboxylic activation. Finally, purified urease dispersed in PB (500 μg, 0.925 nmol) was added to the mixture, which was stirred for 2 h and 30 min at room temperature (see Figure S11 for more details about urease purification). This allowed the covalent immobilization of urease onto the HA-NGs surface via amino groups of lysine with the carboxylic groups of HA.

After the reaction, the resulting NMs were purified to remove the unbound enzyme using a dialysis membrane (MWCO 1000 kD) against PB. The amount of protein attached was quantified using a BCA Protein Assay Kit by measuring the absorbance at 562 nm of the NMs solution with a Synergy HTX Absorbance microplate reader.

4.4. Purification of Urease from *Canavalia ensiformis*. Protein purification was carried out with a fast protein liquid chromatography, NGC Quest 10 Chromatography system, Biorad, as previously reported.[65] Briefly, 90 mg (0.167 μmol) of jack bean urease from *C. ensiformis* (type IX, Sigma-Aldrich catalog no. U4002) was dissolved in PB 1× (300 μL, pH = 7.4). Sample was previously centrifugated at 9400 g for 5 min to remove aggregates and insoluble particles. The protein solution was loaded onto an ENrich SEC 650 10 × 300 size-exclusion column (Biorad cat. no. 780-1650) using a 100 μL loop. The purified urease was collected in fractions of 0.5 mL performing three successive runs, thus collecting 1.5 mL of each fraction.

4.5. Synthesis of MSNPs and MSNP-NMs. MSNPs with an average diameter of 450 nm were produced via a sol−gel process,

modified from the Stöber method.[66] First, CTAB (570 mg, 1.56 mmol) and TEOA (35 g, 0.23 mol) were dissolved in ultrapure water (20 mL) and heated to 95 °C in a silicon oil bath. The reaction took place under reflux and continuous stirring for 30 min. Then, TEOS (1.5 mL, 6.71 mmol) was added slowly with a Pasteur pipet, and the reaction continued for 2 h under the same conditions. The resulting MSNPs were collected by centrifugation at 1350g for 5 min. To remove CTAB, MSNPs were treated with an acidic MeOH solution under reflux. The MSNPs were suspended in MeOH (30 mL), and HCl (1.8 mL, 37%) was added. This mixture was heated in a silicon oil bath at 80 °C for 15 h. Finally, the MSNPs were collected by centrifugation at 1350g for 5 min, followed by three EtOH washes, with 10 min of ultrabath sonication between each centrifugation. The MSNPs were functionalized with APTES to introduce amine groups on their surface. Briefly, APTES (6 μL, 25 μmol) was added to a MSNP suspension (1 mg mL^{-1}) in 70% EtOH. The mixture was heated to 70 °C and stirred for 1 h. Afterward, the resulting MSNP-NH$_2$ were collected by centrifugation and washed three times in EtOH and ultrapure water, with vortexing and sonication between each step. Next, MSNP−NH$_2$ particles (900 μL, 1 mg mL^{-1} in PBS 1×) were activated with GA (100 μL, 0.264 mmol) as a linker for covalent protein binding for 2 h at room temperature on a rotary shaker. After that time, particles were collected, washed in PBS, and resuspended in a solution containing urease (3 mg mL^{-1}) to fabricate the MSNP-NMs. The reaction was left on a rotary shaker overnight at room temperature. The final MSNP-NMs were collected by centrifugation and washed with PBS.

4.6. Hydrodynamic Diameter and Surface Charge. The hydrodynamic diameter, size distribution, and surface charge of HA-NGs, HA-NMs, and MSNP-NMs were measured by DLS using a Zetasizer Nano ZS Malvern Instrument. All measurements were conducted at 25 °C with light scattering detected at 173°, and three replicates were acquired for each condition.

The surface charge of urease was analyzed using UCSF ChimeraX software (UCSF Resource for Biocomputing) employing the Coulombic potential method.

4.7. HA-NMs Enzymatic Activity. The measurements of the apparent Michaelis−Menten constants of HA-NGs NMs and free urease were carried out in 96-well plates in PB at pH 6.5 at room temperature. The enzymatic activity of urease, in free solution and attached to the surface of HA-NGs, was evaluated in the presence of varying urea concentrations. Phenol red, a pH indicator that changes color from yellow to magenta between pH 6.6 and 8.2, was used to monitor the pH increase due to ammonium production during urea hydrolysis. Urea solutions of different concentrations (0, 2.5, 5, 10, 25, 50, 100, 200, and 400 mM) were prepared in aqueous media, with the addition of phenol red indicator (0.04% w/w). Subsequently, PB (2 μL, blank), HA-NGs NMs (2 μL, 1 mg mL^{-1}), or free urease (2 μL, 100 μg mL^{-1}) were mixed with the urea solutions (200 μL). The enzymatic activity was monitored over time by measuring the absorbance at 560 nm for each well using a Synergy HTX Absorbance microplate reader. A phenol red molar extinction coefficient of 31620 M^{-1} cm^{-1} and a path length of 0.5 cm were employed to calculate the activity (U) in μmol s^{-1}. Finally, the curve was fitted to the Michaelis−Menten eq (eq 1)

$$V = V_{max}[urea]/K_m + [urea] \qquad (1)$$

4.8. Transmission and Scanning Electron Microscopy. TEM images were obtained using a JEOL JEM-2100 microscope at 200 kV, equipped with a LaB6 thermionic electron gun, and operated at an accelerating voltage of 200 kV. Images were recorded using a Gatan Orius CCD camera. Data analysis was carried out using the software ImageJ (v.1.53). SEM images were captured by an FEI NOVA NanoSEM 230 instrument at 5 kV. Before SEM observation, the samples were sputter-coated with a 10 nm layer of gold atoms to enhance conductivity, resolution, and contrast. The coating was applied using a Leica EM ACE600 sputter coater with a current strength of 30 mA, resulting in a 10 nm thick coating after 2 min of exposure.

4.9. Single-Particle Tracking and Motion Analysis. The motion of HA-NMs at a single particle level was recorded by using an inverted Leica DMi8 microscope equipped with a Hamamatsu high-speed camera and a 63× water-immersive objective.

Urea solutions (2 μL) were placed on a glass slide and mixed with HA-NMs (2 μL, 20 μg mL^{-1}). The samples were covered with a glass coverslip to avoid artifacts caused by drift. Videos were recorded in bright-field mode for 30 s at a frame rate of 50 FPS. A Python homemade code was used to remove the background and improve the contrast of the videos. Then, an additional Python-based code was used to analyze the videos and obtain the trajectories of HA-NMs. The MSD was calculated using eq 2

$$MSD(\Delta t) = \langle x_i(t + \Delta t) - x_i(t))^2 \rangle \qquad (2)$$

The diffusion coefficient (D_e) was determined by fitting the data to eq 2, which is applicable for small particles with low rotational diffusion at short time intervals. In both cases, 20 particles were analyzed per condition, and the standard error of the mean (SE) was used to calculate the error.

4.10. Collective Displacement and Motion Analysis. The collective displacement of HA-NMs was recorded using optical videos obtained with a Hamamatsu camera attached to a Leica DMi8 inverted fluorescence microscope equipped with a 12.5× objective. A Petri dish was filled with an aqueous urea solution at different concentrations (0, 50, 100 and 200 mM). Then, a drop of HA-NMs (5 μL, 1.5 mg mL^{-1}) was then added to the dish, containing aqueous media with urea. Videos were recorded for 1 min at a frame rate of 20 FPS and posteriorly analyzed with the software ImageJ (v.1.53) to quantify the areal coverage of HA-NMs over time.

4.11. Bacterial Strains and Media. Nonpathogenic strain *E. coli* BL21 DE3 was grown in Luria−Bertani (LB) medium for 24 h at 37 °C (220 rpm). On the next day, bacterial overnight was diluted 1:500 in LB broth (5 mL) and they were grown in LB at 37 °C incubating until the logarithmic phase (OD = 0.6−0.8) was reached before inoculation.

4.12. Confocal Microscopy. HA-NMs were labeled with FITC to enable visualization by confocal microscopy. First, a stock solution of FITC (6 mg mL^{-1}) was prepared by dissolving FITC (6 mg) in DMSO (1 mL). From this stock solution, 50 μL was added to HA-NMs (1 mL, 1.5 mg mL^{-1}) in a light-protected environment. The mixture was continuously stirred overnight to ensure complete labeling. To remove nonencapsulated FITC, the solution was dialyzed against PB (MWCO 14 kD). All steps were protected from light by covering the materials with aluminum foil.

E. coli cells grown in LB liquid medium were incubated with urea (0 or 100 mM) at 37 °C for 2, 24, and 72 h with FITC-labeled HA-NMs at a concentration of 12.5 μg mL^{-1}. After this incubation, bacteria were rinsed twice with PBS 1x to wash away the excess of FITC-labeled HA-NMs. Bacteria were stained with Nile red, a lipophilic cell membrane stain (10 μg mL^{-1}) and DAPI, a DNA-specific fluorescent stain (1 μg mL^{-1}) for 30 min at 37 °C. After that, bacteria were centrifuged at 5000g for 5 min, washed once with PBS, and recentrifuged. Finally, the bacterial pellet was resuspended in a small volume of PBS (50 μL). Bacteria was fixed with 1% paraformaldehyde in ultrapure water for 30 min at room temperature, centrifuged and resuspended in PBS (50 μL). Images were obtained with a confocal microscope (ZEISS LSM 800) by using a 100× oil-immersive objective.

4.13. Chloramphenicol Encapsulation in HA-NMs and MSNP-NMs. MSNP-NMs (0.75 mg) were resuspended in a CHL solution (1 mL, 1 mg mL^{-1}) for drug loading. In contrast, for HA-NMs, an aliquot of HA-NMs (500 μL, 1.5 mg mL^{-1}) was mixed with a CHL solution (500 μL, 2 mg mL^{-1}) in a 1:1 ratio (v/v). The mixtures were incubated for 24 h at room temperature with continuous end-to-end mixing on a rotary shaker. After incubation, the CHL-loaded MSNP-NMs (CHL@ MSNP-NMs) were collected and washed three times by centrifugation to remove the nonloaded drug. For CHL-loaded HA-NMs (CHL@ HA-NMs) the procedure was similar, but the nonloaded drug was removed by filtration using Amicon Eppendorf filters (MWCO 30 kD). Supernatants from both types of NMs were kept and analyzed by measuring the absorbance at 277 nm using a Synergy HTX Absorbance microplate reader to determine the drug-loading capacity and entrapment efficiency of both types of NMs.

4.14. Antibacterial Assays. MICs of NMs were determined using the broth microdilution technique in LB with an initial inoculum of 5 × 10^5 cells mL^{-1} in sterile 96-well polystyrene microplates. Briefly, NMs

were added to the plate as solutions in LB broth at concentrations ranging from 0 to 50 μg mL^{-1}. In the case of free antibiotic, the concentration added was determined by a prior release assay to enable a more accurate comparison. The MIC value was considered the lowest concentration of the antimicrobial system that inhibited the visible growth of bacteria. After 2, 4, 18, and 24 h of incubation at room temperature, the plates were read in a spectrophotometer (Synergy HTX Absorbance microplate reader) at 600 nm. All assays were done in three independent replicates.

4.15. Mucin Crossing Studies. To evaluate the ability of the NMs to penetrate viscous media, a transwell model with a mucin layer was employed to test the capacity of the HA-NMs to cross the mucin barrier. In this setup, the lower chamber was inoculated with *E. coli* at a concentration of 5×10^5 cells mL^{-1} (LB medium, final volume of 600 μL). The upper chamber was coated with a mucin layer (100 μL, 2 wt % in PBS), and urea was added to achieve an equilibrium concentration of 100 mM. Then, a suspension (200 μL) containing free CHL drug (0.867 μg) or NMs loaded with CHL (10 μg) combined with urea (100 mM) was introduced into the upper compartment. Absorbance in the lower chamber was measured at 600 nm using a spectrophotometer (Synergy HTX Absorbance microplate reader) for 4, 8, and 24 h.

■ ASSOCIATED CONTENT

ⓈI Supporting Information

The Supporting Information is available free of charge at https://pubs.acs.org/doi/10.1021/acsami.5c03636.

> Structural modification of HA; structural characterization of HA-based NGs (HA-NGs); optimization of the HA-NPs by self-assembly; structural characterization of HA NG NMs (HA-NMs); characterization of mesoporous silica-based NMs (MSNP-NMs); evaluation of the antimicrobial effect of the chloramphenicol (CHL) loaded into the HA-NMs or MSNP-NMs; internalization assay by confocal microscopy; and urease purification (PDF)
>
> Video S1: Single particle tracking of HA-NMs in the presence or absence of 100 mM urea in aqueous media (MP4)
>
> Video S2: Collective motion of HA-NMs in the presence or absence of 50, 100, and 200 mM of urea in PB, in aqueous media (AVI)

■ AUTHOR INFORMATION

Corresponding Author

Samuel Sánchez − *The Barcelona Institute of Science and Technology (BIST), Institute for Bioengineering of Catalonia (IBEC), 08028 Barcelona, Spain; Catalan Institution for Research and Advanced Studies (ICREA), Passeig Lluís Companys 23, 08010 Barcelona, Spain;* ⓞ orcid.org/0000-0001-9713-9997; Email: ssanchez@ibecbarcelona.eu

Authors

Noelia Ruiz-González − *The Barcelona Institute of Science and Technology (BIST), Institute for Bioengineering of Catalonia (IBEC), 08028 Barcelona, Spain; Facultat de Física, Universitat de Barcelona (UB). C. Martí i Franquès, 08028 Barcelona, Spain;* ⓞ orcid.org/0000-0002-2467-331X

Daniel Sánchez-deAlcázar − *The Barcelona Institute of Science and Technology (BIST), Institute for Bioengineering of Catalonia (IBEC), 08028 Barcelona, Spain; Present Address: Nanobots Therapeutics SL, Baldiri i Reixac 4, 08028 Barcelona, Spain;* ⓞ orcid.org/0000-0001-6034-8525

David Esporrín-Ubieto − *The Barcelona Institute of Science and Technology (BIST), Institute for Bioengineering of*

Catalonia (IBEC), 08028 Barcelona, Spain; ⓞ orcid.org/0000-0002-9858-415X

Valerio Di Carlo − *The Barcelona Institute of Science and Technology (BIST), Institute for Bioengineering of Catalonia (IBEC), 08028 Barcelona, Spain;* ⓞ orcid.org/0000-0002-5099-0685

Complete contact information is available at:
https://pubs.acs.org/10.1021/acsami.5c03636

Author Contributions

[⊥]N.R.G. and D.S.dA. contributed equally to this work. N.R.G. optimized the synthesis of HA self-assembly NPs, HA-NGs, and NMs. She also conducted DLS, z-potential, single-particle motion, and collective motion measurements. D.S.dA. conducted bacterial experiments, protein purification, and enzymatic activity assays. D.E.U. provided scientific guidance and supervision for the preparation of NMs and performed SEM, NMR, FTIR, and collective motion characterizations. V.D.C. carried out confocal microscopy experiments. N.R.G. wrote the first draft of the manuscript. D.S.dA., D.E.U., V.D.C., and S.S. improved the manuscript. S.S. supervised and administered the work. All authors have reviewed and approved the final version of the manuscript.

Notes

The authors declare no competing financial interest.

■ ACKNOWLEDGMENTS

■ REFERENCES

(1) *Antimicrobial Resistance.* https://www.who.int/news-room/fact-sheets/detail/antimicrobial-resistance (accessed 2024−10−26).

(2) Baquero, F. Threats of Antibiotic Resistance: An Obliged Reappraisal. *Int. Microbiol.* **2021**, *24* (4), 499−506.

(3) Bryers, J. D. Medical Biofilms. *Biotechnol. Bioeng.* **2008**, *100* (1), 1−18.

(4) Laxminarayan, R.; Duse, A.; Wattal, C.; Zaidi, A. K. M.; Wertheim, H. F. L.; Sumpradit, N.; Vlieghe, E.; Hara, G. L.; Gould, I. M.; Goossens, H.; Greko, C.; So, A. D.; Bigdeli, M.; Tomson, G.; Woodhouse, W.; Ombaka, E.; Peralta, A. Q.; Qamar, F. N.; Mir, F.;

Kariuki, S.; Bhutta, Z. A.; Coates, A.; Bergstrom, R.; Wright, G. D.; Brown, E. D.; Cars, O. Antibiotic Resistance—the Need for Global Solutions. *Lancet Infect. Dis.* **2013**, *13* (12), 1057−1098.

(5) Tse, B. N.; Adalja, A. A.; Houchens, C.; Larsen, J.; Inglesby, T. V.; Hatchett, R. Challenges and Opportunities of Nontraditional Approaches to Treating Bacterial Infections. *Clin. Infect. Dis.* **2017**, *65* (3), 495−500.

(6) Kalelkar, P. P.; Riddick, M.; García, A. J. Biomaterial-Based Antimicrobial Therapies for the Treatment of Bacterial Infections. *Nat. Rev. Mater.* **2022**, *7* (1), 39−54.

(7) Tuson, H. H.; Weibel, D. B. Bacteria-Surface Interactions. *Soft Matter* **2013**, *9* (18), 4368−4380.

(8) Boegh, M.; Nielsen, H. M. Mucus as a Barrier to Drug Delivery − Understanding and Mimicking the Barrier Properties. *Basic Clin. Pharmacol. Toxicol.* **2015**, *116* (3), 179−186.

(9) Khan, J.; Tarar, S. M.; Gul, I.; Nawaz, U.; Arshad, M. Challenges of Antibiotic Resistance Biofilms and Potential Combating Strategies: A Review. *3 Biotech* **2021**, *11* (4), 169.

(10) Jia, J.; Wang, Z.; Yue, T.; Su, G.; Teng, C.; Yan, B. Crossing Biological Barriers by Engineered Nanoparticles. *Chem. Res. Toxicol.* **2020**, *33* (5), 1055−1060.

(11) Ramos Docampo, M. A. On Nanomachines and Their Future Perspectives in Biomedicine. *Adv. Biol.* **2023**, *7* (4), 2200308.

(12) Liu, W.; Liu, Y.; Li, H.; Nie, H.; Tian, M.; Long, W. Biomedical Micro-/Nanomotors: Design, Imaging, and Disease Treatment. *Adv. Funct. Mater.* **2023**, *33* (15), 2212452.

(13) Hortelão, A. C.; Patiño, T.; Perez-Jiménez, A.; Blanco, A.·.; Sánchez, S. Enzyme-Powered Nanobots Enhance Anticancer Drug Delivery. *Adv. Funct. Mater.* **2018**, *28* (25), 1705086.

(14) de Ávila, B. E.-F.; Angsantikul, P.; Li, J.; Angel Lopez-Ramirez, M.; Ramírez-Herrera, D. E.; Thamphiwatana, S.; Chen, C.; Delezuk, J.; Samakapiruk, R.; Ramez, V.; Obonyo, M.; Zhang, L.; Wang, J. Micromotor-Enabled Active Drug Delivery for in Vivo Treatment of Stomach Infection. *Nat. Commun.* **2017**, *8* (1), 272.

(15) Zhang, Z.; Zhang, D.; Qiu, B.; Cao, W.; Liu, Y.; Liu, Q.; Li, X. Icebreaker-Inspired Janus Nanomotors to Combat Barriers in the Delivery of Chemotherapeutic Agents. *Nanoscale* **2021**, *13* (13), 6545−6557.

(16) Ramos-Docampo, M. A.; Fernández-Medina, M.; Taipaleenmäki, E.; Hovorka, O.; Salgueiriño, V.; Städler, B. Microswimmers with Heat Delivery Capacity for 3D Cell Spheroid Penetration. *ACS Nano* **2019**, *13* (10), 12192−12205.

(17) Hortelao, A. C.; Carrascosa, R.; Murillo-Cremaes, N.; Patino, T.; Sánchez, S. Targeting 3D Bladder Cancer Spheroids with Urease-Powered Nanomotors. *ACS Nano* **2019**, *13* (1), 429−439.

(18) Chen, W.; Jiang, R.; Sun, X.; Chen, S.; Liu, X.; Fu, M.; Yan, X.; Ma, X. Self-Fueled Janus Nanomotors as Active Drug Carriers for Propulsion Behavior-Reinforced Permeability and Accumulation at the Tumor Site. *Chem. Mater.* **2022**, *34* (16), 7543−7552.

(19) Ramos Docampo, M. A.; Wang, N.; Pendlmayr, S.; Städler, B. Self-Propelled Collagenase-Powered Nano/Micromotors. *ACS Appl. Nano Mater.* **2022**, *5* (10), 14622−14629.

(20) Fraire, J. C.; Guix, M.; Hortelao, A. C.; Ruiz-González, N.; Bakenecker, A. C.; Ramezani, P.; Hinnekens, C.; Sauvage, F.; De Smedt, S. C.; Braeckmans, K.; Sánchez, S. Light-Triggered Mechanical Disruption of Extracellular Barriers by Swarms of Enzyme-Powered Nanomotors for Enhanced Delivery. *ACS Nano* **2023**, *17* (8), 7180−7193.

(21) Llopis-Lorente, A.; García-Fernández, A.; Murillo-Cremaes, N.; Hortelão, A. C.; Patiño, T.; Villalonga, R.; Sancenón, F.; Martínez-Máñez, R.; Sánchez, S. Enzyme-Powered Gated Mesoporous Silica Nanomotors for On-Command Intracellular Payload Delivery. *ACS Nano* **2019**, *13* (10), 12171−12183.

(22) Zhang, X.; Chen, C.; Wu, J.; Ju, H. Bubble-Propelled Jellyfish-like Micromotors for DNA Sensing. *ACS Appl. Mater. Interfaces* **2019**, *11* (14), 13581−13588.

(23) Yang, Y.; Arqué, X.; Patiño, T.; Guillerm, V.; Blersch, P.-R.; Pérez-Carvajal, J.; Imaz, I.; Maspoch, D.; Sánchez, S. Enzyme-Powered Porous Micromotors Built from a Hierarchical Micro- and Mesoporous

UiO-Type Metal−Organic Framework. *J. Am. Chem. Soc.* **2020**, *142* (50), 20962−20967.

(24) Ma, X.; Jannasch, A.; Albrecht, U. R.; Hahn, K.; Miguel-López, A.; Schäffer, E.; Sánchez, S. Enzyme-Powered Hollow Mesoporous Janus Nanomotors. *Nano Lett.* **2015**, *15* (10), 7043−7050.

(25) Arqué, X.; Romero-Rivera, A.; Feixas, F.; Patiño, T.; Osuna, S.; Sánchez, S. Intrinsic Enzymatic Properties Modulate the Self-Propulsion of Micromotors. *Nat. Commun.* **2019**, *10* (1), 2826.

(26) Ruiz-González, N.; Esporrín-Ubieto, D.; Hortelao, A. C.; Fraire, J. C.; Bakenecker, A. C.; Guri-Canals, M.; Cugat, R.; Carrillo, J. M.; Garcia-Batlletbó, M.; Laiz, P.; Patiño, T.; Sánchez, S. Swarms of Enzyme-Powered Nanomotors Enhance the Diffusion of Macromolecules in Viscous Media. *Small* **2024**, *20* (11), 2309387.

(27) Hortelao, A. C.; Simó, C.; Guix, M.; Guallar-Garrido, S.; Julián, E.; Vilela, D.; Rejc, L.; Ramos-Cabrer, P.; Cossío, U.; Gómez-Vallejo, V.; Patiño, T.; Llop, J.; Sánchez, S. Swarming Behavior and in Vivo Monitoring of Enzymatic Nanomotors within the Bladder. *Sci. Robot.* **2021**, *6* (52), 2823.

(28) Simó, C.; Serra-Casablancas, M.; Hortelao, A. C.; Di Carlo, V.; Guallar-Garrido, S.; Plaza-García, S.; Rabanal, R. M.; Ramos-Cabrer, P.; Yagüe, B.; Aguado, L.; Bardia, L.; Tosi, S.; Gómez-Vallejo, V.; Martín, A.; Patiño, T.; Julián, E.; Colombelli, J.; Llop, J.; Sánchez, S. Urease-Powered Nanobots for Radionuclide Bladder Cancer Therapy. *Nat. Nanotechnol.* **2024**, *19* (4), 554−564.

(29) Serra-Casablancas, M.; Di Carlo, V.; Esporrín-Ubieto, D.; Prado-Morales, C.; Bakenecker, A. C.; Sánchez, S. Catalase-Powered Nanobots for Overcoming the Mucus Barrier. *ACS Nano* **2024**, *18* (26), 16701−16714.

(30) Hortelão, A. C.; García-Jimeno, S.; Cano-Sarabia, M.; Patiño, T.; Maspoch, D.; Sanchez, S. LipoBots: Using Liposomal Vesicles as Protective Shell of Urease-Based Nanomotors. *Adv. Funct. Mater.* **2020**, *30* (42), 1−8.

(31) Wang, J.; Wu, H.; Zhu, X.; Zwolsman, R.; Hofstraat, S. R. J.; Li, Y.; Luo, Y.; Joosten, R. R. M.; Friedrich, H.; Cao, S.; Abdelmohsen, L. K. E. A.; Shao, J.; van Hest, J. C. M. Ultrafast Light-Activated Polymeric Nanomotors. *Nat. Commun.* **2024**, *15* (1), 4878.

(32) Somasundar, A.; Ghosh, S.; Mohajerani, F.; Massenburg, L. N.; Yang, T.; Cremer, P. S.; Velegol, D.; Sen, A. Positive and Negative Chemotaxis of Enzyme-Coated Liposome Motors. *Nat. Nanotechnol.* **2019**, *14* (12), 1129−1134.

(33) Fraire, J. C.; Prado-Morales, C.; Aldaz Sagredo, A.; Caelles, A. G.; Lezcano, F.; Peetroons, X.; Bakenecker, A. C.; Di Carlo, V.; Sánchez, S. Swarms of Enzymatic Nanobots for Efficient Gene Delivery. *ACS Appl. Mater. Interfaces* **2024**, *16* (36), 47192−47205.

(34) Wang, J.; Liu, J.; Sümbelli, Y.; Shao, J.; Shi, X.; van Hest, J. C. M. Nanogel-Based Nitric Oxide-Driven Nanomotor for Deep Tissue Penetration and Enhanced Tumor Therapy. *J. Controlled Release* **2024**, *372*, 59−68.

(35) Joseph, A.; Contini, C.; Cecchin, D.; Nyberg, S.; Ruiz-Perez, L.; Gaitzsch, J.; Fullstone, G.; Tian, X.; Azizi, J.; Preston, J.; Volpe, G.; Battaglia, G. Chemotactic Synthetic Vesicles: Design and Applications in Blood-Brain Barrier Crossing. *Sci. Adv.* **2017**, *3* (8), No. e1700362.

(36) Kamaly, N.; Xiao, Z.; Valencia, P. M.; Radovic-Moreno, A. F.; Farokhzad, O. C. Targeted Polymeric Therapeutic Nanoparticles: Design, Development and Clinical Translation. *Chem. Soc. Rev.* **2012**, *41* (7), 2971.

(37) Ariga, K. Nanoarchitectonics: The Method for Everything in Materials Science. *Bull. Chem. Soc. Jpn.* **2024**, *97* (1), uoad001.

(38) Jancik-Prochazkova, A.; Ariga, K. Nano-/Microrobots for Environmental Remediation in the Eyes of Nanoarchitectonics: Toward Engineering on a Single-Atomic Scale. *Research* **2025**, *8*, 0624.

(39) Hamidi, M.; Azadi, A.; Rafiei, P. Hydrogel Nanoparticles in Drug Delivery. *Adv. Drug Delivery Rev.* **2008**, *60* (15), 1638−1649.

(40) Ahmed, E. M. Hydrogel: Preparation, Characterization, and Applications: A Review. *J. Adv. Res.* **2015**, *6* (2), 105−121.

(41) Kabanov, A. V.; Vinogradov, S. V. Nanogels as Pharmaceutical Carriers: Finite Networks of Infinite Capabilities. *Angew. Chem., Int. Ed.* **2009**, *48* (30), 5418−5429.

(42) Iaconisi, G. N.; Lunetti, P.; Gallo, N.; Cappello, A. R.; Fiermonte, G.; Dolce, V.; Capobianco, L. Hyaluronic Acid: A Powerful Biomolecule with Wide-Ranging Applications—A Comprehensive Review. *Int. J. Mol. Sci.* **2023**, *24* (12), 10296.

(43) Salih, A. R. C.; Farooqi, H. M. U.; Amin, H.; Karn, P. R.; Meghani, N.; Nagendran, S. Hyaluronic Acid: Comprehensive Review of a Multifunctional Biopolymer. *Futur J. Pharm. Sci.* **2024**, *10* (1), 63.

(44) Choi, K. Y.; Saravanakumar, G.; Park, J. H.; Park, K. Hyaluronic Acid-Based Nanocarriers for Intracellular Targeting: Interfacial Interactions with Proteins in Cancer. *Colloids Surf., B* **2012**, *99*, 82−94.

(45) Myint, S. S.; Laomeephol, C.; Thamnium, S.; Chamni, S.; Luckanagul, J. A. Hyaluronic Acid Nanogels: A Promising Platform for Therapeutic and Theranostic Applications. *Pharmaceutics* **2023**, *15* (12), 2671.

(46) Stanton, M. M.; Park, B.-W.; Vilela, D.; Bente, K.; Faivre, D.; Sitti, M.; Sánchez, S. Magnetotactic Bacteria Powered Biohybrids Target E. Coli Biofilms. *ACS Nano* **2017**, *11* (10), 9968−9978.

(47) Vilela, D.; Blanco-Cabra, N.; Eguskiza, A.; Hortelao, A. C.; Torrents, E.; Sanchez, S. Drug-Free Enzyme-Based Bactericidal Nanomotors against Pathogenic Bacteria. *ACS Appl. Mater. Interfaces* **2021**, *13* (13), 14964−14973.

(48) Arqué, X.; Torres, M. D. T.; Patiño, T.; Boaro, A.; Sánchez, S.; de la Fuente-Nunez, C. Autonomous Treatment of Bacterial Infections in Vivo Using Antimicrobial Micro- and Nanomotors. *ACS Nano* **2022**, *16* (5), 7547−7558.

(49) Wang, H.; Chen, X.; Zhang, L.; Han, Z.; Zheng, J.; Qi, Y.; Zhao, W.; Xu, X.; Li, T.; Zhou, Y.; Bao, P.; Xue, X. Dual-Fuel Propelled Nanomotors with Two-Stage Permeation for Deep Bacterial Infection in the Treatment of Pulpitis. *Advanced Science* **2024**, *11* (5), 2305063.

(50) Liu, L.; Li, S.; Yang, K.; Chen, Z.; Li, Q.; Zheng, L.; Wu, Z.; Zhang, X.; Su, L.; Wu, Y.; Song, J. Drug-Free Antimicrobial Nanomotor for Precise Treatment of Multidrug-Resistant Bacterial Infections. *Nano Lett.* **2023**, *23* (9), 3929−3938.

(51) Shariati, M.; Lollo, G.; Matha, K.; Descamps, B.; Vanhove, C.; Van de Sande, L.; Willaert, W.; Balcaen, L.; Vanhaecke, F.; Benoit, J.-P.; Ceelen, W.; De Smedt, S. C.; Remaut, K. Synergy between Intraperitoneal Aerosolization (PIPAC) and Cancer Nanomedicine: Cisplatin-Loaded Polyarginine-Hyaluronic Acid Nanocarriers Efficiently Eradicate Peritoneal Metastasis of Advanced Human Ovarian Cancer. *ACS Appl. Mater. Interfaces* **2020**, *12* (26), 29024−29036.

(52) Patiño, T.; Feiner-Gracia, N.; Arqué, X.; Miguel-López, A.; Jannasch, A.; Stumpp, T.; Schäffer, E.; Albertazzi, L.; Sánchez, S. Influence of Enzyme Quantity and Distribution on the Self-Propulsion of Non-Janus Urease-Powered Micromotors. *J. Am. Chem. Soc.* **2018**, *140* (25), 7896−7903.

(53) Hanefeld, U.; Gardossi, L.; Magner, E. Understanding Enzyme Immobilisation. *Chem. Soc. Rev.* **2009**, *38* (2), 453−468.

(54) Patiño, T.; Arqué, X.; Mestre, R.; Palacios, L.; Sánchez, S. Fundamental Aspects of Enzyme-Powered Micro- and Nanoswimmers. *Acc. Chem. Res.* **2018**, *51* (11), 2662−2671.

(55) Toebes, B. J.; Abdelmohsen, L. K. E. A.; Wilson, D. A. Enzyme-Driven Biodegradable Nanomotor Based on Tubular-Shaped Polymeric Vesicles. *Polym. Chem.* **2018**, *9* (23), 3190−3194.

(56) Simmchen, J.; Baeza, A.; Ruiz-Molina, D.; Vallet-Regí, M. Improving Catalase-Based Propelled Motor Endurance by Enzyme Encapsulation. *Nanoscale* **2014**, *6* (15), 8907−8913.

(57) Wang, S.; Xu, D.; Liu, X.; Wang, Y.; Ye, H.; Ma, X. Improving Thermal Stability of Enzymatic Micromotors by a Temperature-Sensitive Smart Polymeric Shell. *ChemNanoMat* **2022**, *8* (4), No. e202100447.

(58) Patiño, T.; Llacer-Wintle, J.; Pujals, S.; Albertazzi, L.; Sánchez, S. Unveiling Protein Corona Formation around Self-Propelled Enzyme Nanomotors by Nanoscopy. *Nanoscale* **2024**, *16* (6), 2904−2912.

(59) Chen, S.; Peetroons, X.; Bakenecker, A. C.; Lezcano, F.; Aranson, I. S.; Sánchez, S. Collective Buoyancy-Driven Dynamics in Swarming Enzymatic Nanomotors. *Nat. Commun.* **2024**, *15* (1), 1−12.

(60) Oong, G. C.; Tadi, P. Chloramphenicol - StatPearls - NCBI Bookshelf. https://www.ncbi.nlm.nih.gov/books/NBK555966/ (accessed 2024−10−02).

(61) Murgia, X.; Loretz, B.; Hartwig, O.; Hittinger, M.; Lehr, C. M. The Role of Mucus on Drug Transport and Its Potential to Affect Therapeutic Outcomes. *Adv. Drug Delivery Rev.* **2018**, *124*, 82−97.

(62) Eckmann, D. M.; Composto, R. J.; Tsourkas, A.; Muzykantov, V. R. Nanogel Carrier Design for Targeted Drug Delivery. *J. Mater. Chem. B* **2014**, *2* (46), 8085−8097.

(63) Yang, C.; Wang, X.; Yao, X.; Zhang, Y.; Wu, W.; Jiang, X. Hyaluronic Acid Nanogels with Enzyme-Sensitive Cross-Linking Group for Drug Delivery. *J. Controlled Release* **2015**, *205*, 206−217.

(64) Butnarasu, C.; Barbero, N.; Pacheco, D.; Petrini, P.; Visentin, S. Mucin Binding to Therapeutic Molecules: The Case of Antimicrobial Agents Used in Cystic Fibrosis. *Int. J. Pharm.* **2019**, *564*, 136−144.

(65) Valles, M.; Pujals, S.; Albertazzi, L.; Sánchez, S. Enzyme Purification Improves the Enzyme Loading, Self-Propulsion, and Endurance Performance of Micromotors. *ACS Nano* **2022**, *16* (4), 5615−5626.

(66) Stöber, W.; Fink, A.; Bohn, E. Controlled Growth of Monodisperse Silica Spheres in the Micron Size Range. *J. Colloid Interface Sci.* **1968**, *26* (1), 62−69.